Effects of ITCZ Poleward Location Bias on ENSO Seasonal Phase-Locking Simulation in Climate Models

HUAXIA LIAO,[a] ZHICHAO CAI,[a] JINGSONG GUO,[b,c] AND ZHENYA SONG[b,c]

[a] *School of Basic Sciences for Aviation, Naval Aviation University, Yantai, Shandong, China*
[b] *First Institute of Oceanography, Key Laboratory of Marine Science and Numerical Modeling, Ministry of Natural Resources, Qingdao, Shandong, China*
[c] *Shandong Key Laboratory of Marine Science and Numerical Modeling, Qingdao, Shandong, China*

(Manuscript received 1 December 2022, in final form 9 April 2023, accepted 11 April 2023)

ABSTRACT: El Niño–Southern Oscillation (ENSO) is the most influential interannual climate variability on Earth. The tendency of the mature phase of ENSO, characterized by the strongest sea surface temperature (SST) anomalies, to appear during the boreal winter is known as seasonal phase locking. Climate models are challenged by biases in simulating ENSO seasonal phase locking. Here, we evaluated the ENSO phase-locking simulation performance in 50 models of phase 6 of the Coupled Model Intercomparison Project (CMIP6) and found that the models with the intertropical convergence zone (ITCZ) poleward bias tended to simulate more ENSO events that peaked out of the boreal winter season. The contributions of the ITCZ poleward bias to the ENSO phase-locking bias were also evaluated, yielding a correlation coefficient of 0.55, which can explain approximately 30% of the ENSO seasonal phase-locking bias. The mechanism that influences the simulation of ENSO seasonal phase locking was also assessed. The ITCZ poleward bias induces a dry bias over the equatorial Pacific, especially during the boreal summer. During ENSO events, the meridional movement of the ITCZ is prevented, and the equatorial precipitation and convection anomalies that respond to ENSO events are also restrained. The restrained convection anomaly weakens the ENSO-related zonal wind anomaly, triggering a weaker eastern tropical Pacific thermocline anomaly during the following autumn. The weakened thermocline anomaly cannot sustain further development of ENSO-related SST anomalies. Therefore, ENSO events in models containing the ITCZ poleward bias are restrained during the boreal summer and autumn and, thus, tend to peak out of the winter season.

SIGNIFICANCE STATEMENT: We aimed to better understand the mechanism that induces bias when simulating ENSO seasonal phase locking, that is, what disturbs the simulated ENSO events peaking during the boreal winter. As previous studies have primarily focused on the South Pacific convergence zone (SPCZ) bias and other biases, this study is the first to propose the effects of the poleward ITCZ latitude bias and clarify the corresponding mechanism. We show that latitudinal bias can explain approximately 30% of the ENSO seasonal phase-locking bias. This is important because the biases in simulating ENSO seasonal phase locking have long hampered the prediction of ENSO. Our study highlights the importance of the latitude of the ITCZ and provides a basis for the future development of climate models.

KEYWORDS: ENSO; Climate models; Intertropical convergence zone

1. Introduction

Characterized by significant changes in sea temperature and atmospheric circulation, El Niño–Southern Oscillation (ENSO) is recognized as the most influential interannual climate variability on Earth (Philander 1983; Wang and Picaut 2004). The mature phase of ENSO, with the strongest sea surface temperature (SST) and atmospheric circulation anomalies, usually appears in the boreal winter (Mitchell and Wallace 1996; Neelin et al. 2000), and climatologists refer to this phenomenon as seasonal phase locking. Climate models and their ability to simulate ENSO events are important tools for studying and predicting ENSO events (Fang et al. 2019; Levine and McPhaden 2015; Zheng and Zhu 2010); however, the bias in simulating ENSO seasonal phase locking remains a challenge for existing climate models (Bellenger et al. 2014; Chen et al. 2019; Ham and Kug 2014b; Rashid and Hirst 2016). Phase 6 of the Coupled Model Intercomparison Project (CMIP6) (Eyring et al. 2016) provides an excellent opportunity to assess the ENSO phase-locking simulation ability of state-of-the-art climate models. Recent studies suggest that, even though the ability to simulate ENSO seasonal phase locking has improved

Denotes content that is immediately available upon publication as open access.

Corresponding author: Zhenya Song, songroy@fio.org.cn

DOI: 10.1175/JCLI-D-22-0891.1

slightly from CMIP5 to CMIP6, many CMIP6 models still simulate the mature phase of ENSO as occurring outside of the winter season (Chen and Jin 2021, 2022; Liao et al. 2021). Therefore, a better understanding of the mechanisms of ENSO seasonal phase locking in climate models is needed.

The zonal surface wind anomaly that responds to ENSO is essential for seasonal phase locking (Abellán and McGregor 2016). During El Niño events, in response to the positive SST anomaly, a westerly wind anomaly appears over the western tropical Pacific. The westerly wind anomaly deepens the thermocline in the eastern tropical Pacific, amplifying the SST anomaly and maintaining the development of ENSO events (Jin 1997a,b; Suarez and Schopf 1988). A similar process occurs during the La Niña events as well. This positive feedback is the so-called Bjerknes feedback (Bjerknes 1969). Since the intertropical convergence zone (ITCZ) reaches its northernmost and southernmost positions in September and March–April (Xie and Carton 2004), respectively, the meridional displacement of the climatological ITCZ leads the annual cycle in equatorial SST in the Pacific Ocean by maintaining southerly cross-equatorial winds that intensify in the boreal summer/fall and relax in the boreal spring (Li and Philander 1996; Mitchell and Wallace 1992; Xie 1994). During the boreal summer and fall, the strong equatorial zonal SST gradient and easterly trade wind, together with the shallower thermocline depth in the eastern tropical Pacific, amplify the sensibility of the SST anomaly responses to the zonal surface wind anomaly. However, during boreal spring, the response turns insensitive due to the weakened zonal SST gradient, the relaxed surface trade wind, and the deepened thermocline depth. Therefore, the Bjerknes feedback is stronger during the boreal summer and autumn but weaker during the boreal spring (Abellán et al. 2017). The instability of ENSO changes synchronously with the strength of the Bjerknes feedback (Jin et al. 2006). The ENSO SST anomaly usually develops during the boreal summer and autumn, when the Bjerknes feedback is strong and robust. In contrast, under the effect of damping processes, such as the surface net heat flux (Huang et al. 2010), it decays during the boreal spring, when the Bjerknes feedback is weak and fragile. Thus, it favors the winter peaking of ENSO events (Dippe et al. 2019).

In climate models, the inaccurate simulation of ENSO-related wind anomalies is linked to the unrealistic distribution of SST. These biases disturb the seasonal variation of ENSO instability and lead to the inaccurate simulation of ENSO seasonal phase locking. Previous studies have identified that the surface winds that respond to zonal SST variability are too weak in the CMIP3 and CMIP5 models (Bellenger et al. 2014; Kim et al. 2014). Surface wind bias affects the thermocline and zonal advective feedback over the tropical Pacific, thus modulating ENSO instability (Kim et al. 2014). Furthermore, models with colder equatorial SST, weaker surface wind, and convection during the boreal summer also tend to produce summer-peaking ENSO events (Ham and Kug 2014b; Ham et al. 2012).

In addition to SST, other components can affect ENSO-related wind anomalies (Choi et al. 2015). For example, the pressure gradient anomaly that generates surface wind anomalies over the tropical Pacific arises from two components: the SST gradient anomaly (Lindzen and Nigam 1987) and the deep convection anomaly (Deser and Wallace 1990; Gill 1980). The former is largely related to the expansion of the Pacific cold tongue, while the latter is usually associated with the strength and movement of the ITCZ and South Pacific convergence zone (SPCZ) (Adam 2018; Chiang et al. 2001; Park et al. 2021; Xie et al. 2018). McGregor et al. (2012) pointed out that the southward shift of ENSO-related zonal wind anomalies during the boreal winter and spring is highly associated with the SPCZ. The southward shift of the zonal wind anomaly reduces the ENSO-related zonal wind response over the equator and, thus, seasonally terminates strong El Niño events during the boreal spring (McGregor et al. 2012). Therefore, the realistic simulation of the SPCZ and the associated convection greatly impact the synchronization of simulated ENSO events with the seasonal cycle (McGregor et al. 2013).

As the primary convection over the tropical Pacific north of the equator, the ITCZ also plays an important role in the simulation of ENSO events. Previous studies found that climate models with a stronger central-eastern Pacific ITCZ tend to simulate eastward and northward expansion of ENSO-related wind stress, thus leading to a slower ENSO phase transition (Ham and Kug 2014a). Stronger convection, a wetter ITCZ, and drier conditions over the Pacific cold tongue shift the ENSO-related atmospheric responses westward, thereby modulating the strength of the Bjerknes feedback and controlling the amplitude of ENSO events (Watanabe et al. 2011). In addition, the meridional location of the ITCZ can modulate the relationship between the North Pacific Oscillation (NPO) and ENSO (Park et al. 2021; Zheng et al. 2021). However, whether the simulation of the ITCZ can influence ENSO seasonal phase-locking performance (PLP) in climate models remains undetermined.

Liao et al. (2021) proposed a new index that can evaluate the ability of a model to simulate ENSO seasonal phase locking through the proportion of winter-peaking El Niño events (Fig. 1a). Based on this index, we evaluated the ENSO seasonal phase-locking performance of 50 CMIP6 models. We identify significant connections with a climatological ITCZ (Fig. 1d), with significant positive and negative correlations south and north of the observed ITCZ locations, respectively. This meridional dipole pattern is usually associated with the northward bias of the mean ITCZ position (Chiang and Vimont 2004). Therefore, it seems that the models with the northward bias of the mean ITCZ position tend to simulate weaker ENSO seasonal phase locking (Fig. 1b). As there are still several systematic ITCZ errors among the CMIP6 models, the ensemble mean of precipitation extends too far north and too wide over the northern tropical Pacific (Si et al. 2021; Tian and Dong 2020). Thus, it is necessary to determine how the mean ITCZ position affects the seasonal synchronization of ENSO.

The remainder of this paper is organized as follows. A brief description of the datasets and analysis methods is presented in section 2. Section 3 classifies the CMIP6 models into different ensembles based on ITCZ mean meridional location and verifies the connection between the simulated ITCZ and

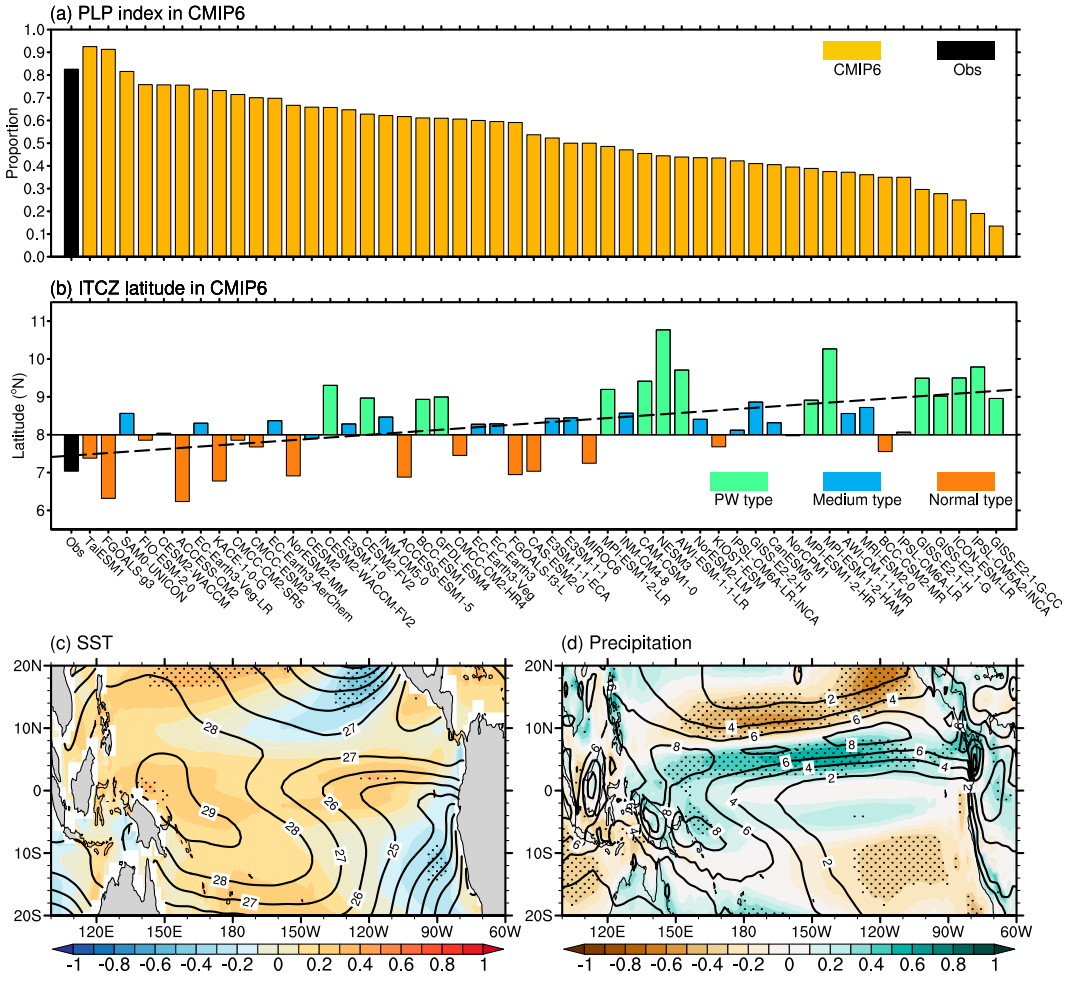

FIG. 1. Model performance when simulating ENSO seasonal phase locking and the connections with the tropical background: (a) phase-locking performance (PLP) index and (b) ITCZ latitude in observations and each CMIP6 model. Models in (b) are classified as normal type (orange), medium type (light blue), or poleward (PW) type (light green) based on the ITCZ latitude. Black dashed line in (b) indicates regression between the simulated PLP index and ITCZ latitudes. Also shown are correlation coefficients (shading) between the PLP index and (c) SST or (d) precipitation over the tropical Pacific Ocean based on the CMIP6 model ensemble. The observed climatological SST and precipitation are shown as contours in (c) and (d), respectively. Stippling represents the regions in which the correlation is statistically significant at the 95% confidence level.

ENSO seasonal phase locking. This section also evaluates the contribution of the simulated ITCZ to ENSO seasonal phase-locking biases. Section 4 analyzes the mechanism that disturbs the simulated ENSO seasonal phase locking by comparing the different CMIP6 ensembles proposed in section 3. In section 5, we provide a discussion of our results and present our conclusions.

2. Data and methodology

a. Observational and model datasets

We used the following observational datasets: SST data from the Extended Reconstructed Sea Surface Temperature (ERSST), version 5, available since 1854 on a 2° × 2° grid (Huang et al. 2017); precipitation data from the Global Precipitation Climatology Project (GPCP) monthly analysis product, version 2.3, available since 1979 on a 1° × 1° grid (Adler et al. 2018); and surface wind stress data, seawater zonal velocity data, and seawater potential temperature data from the Global Ocean Data Assimilation System (GODAS) monthly products, available since 1980 on a 1° × 0.33° grid (Behringer and Xue 2004). Thermocline data at 15°C isothermal depth were also calculated based on seawater potential temperature data. The mixed layer zonal velocity data were calculated based on the seawater zonal velocity data, while the mixed layer depth was defined as the depth at which the ocean temperature deviates 0.5°C from SST (Huang et al. 2010).

The simulated monthly SST, precipitation, zonal surface wind stress, seawater zonal velocity, and seawater potential temperature data were from the first realization of the

historical simulation (r1i1p1f1) of CMIP6 climate models (Eyring et al. 2016). The CMIP historical simulation branches from the preindustrial control simulation spin-up experiment, forced by observed externally imposed forcings after the industrial revolution, such as solar, volcanic, aerosol, and greenhouse gas data. This was integrated from 1850 and extended to 2014 in CMIP6. Owing to the gradually enriched observational datasets, the CMIP historical simulation provides rich opportunities for assessing model simulation ability. Table 1 summarizes information for the 50 CMIP6 climate models available at the time of writing. All CMIP6 data are analyzed for 1870–2014. Note that the seawater potential temperature data in the Korea Meteorological Administration Advanced Community Earth System (KACE) model (KACE-1-0-G), NorESM2-LM model, and NorESM2-MM model, and the seawater zonal velocity data in the CAS-ESM2-0, CMCC-CM2-HR4, KACE-1-0-G, NorESM2-MM, and GFDL-ESM4 models, were unavailable until the investigation was complete.

b. Methods

The Niño-3 index (SST anomaly averaged over 5°S–5°N, 150°–90°W) was used to select ENSO events. For each Niño-3 time series in both the observations and models, the long-term linear trend was first removed (Lindsey 2013), and then a 3-month running average was applied as a preprocessing step. El Niño and La Niña events were then selected as those periods when positive and negative values of the Niño-3 index exceeded 0.5 times the standard deviation (SD) of the time series, for a period of more than 6 months, respectively (Levine et al. 2016). The ENSO seasonal phase-locking performance of each model was detected as the proportion of winter-peaking El Niño events out of all El Niño events (Guilyardi et al. 2003; Liao et al. 2021), where winter-peaking El Niño events are defined as those events peaking around the boreal winter (October–February). We defined the proportion of winter-peaking El Niño events as the PLP index (Fig. 1a). A model with a higher PLP index indicates stronger ENSO seasonal phase locking. Note that it is generally believed that ENSO usually peaks in November—January (Deser et al. 2010), but there is still a certain amount of ENSO event peak in October and February. The possibility that ENSO peaks in October and February is smaller than that for November, December, and January but is much larger than the possibility in other months (Chen and Jin 2021). Besides, since the simulated ENSO phase-locking bias is associated with multiple factors, the connections between the ENSO phase-locking bias and a single factor can be disturbed or hidden by other factors. Those disturbers can be partly excluded by properly broadening the ENSO phase-locking time range. We further checked the connections between the mean state components and the PLP index, which is based on the time range from November to January. Based on the shorter time range, there are still obvious connections between the ITCZ and the PLP index. We also checked the PLP index based on the Niño-3.4 index (SST anomaly averaged over 5°S–5°N, 170°–120°W) and found similar but weaker connections with the simulated ITCZ. This slight difference may be due to the better seasonal phase-locking performance of the Niño-3.4 SST anomaly, which is caused by the better simulation of zonal advection feedback in that region (Chen and Jin 2022).

The meridional location and magnitude of the ITCZ were represented by the latitude and strength of the maximum precipitation over the central Pacific (CP). The precipitation was first zonally averaged over 160°–240°E, and then a weighting function was performed to identify the latitude of the precipitation maximum over the northern tropical Pacific (Adam et al. 2016). The latitude of the precipitation maximum was calculated as follows:

$$\phi_{\mathrm{ITCZ}} = \frac{\int_{\phi_1}^{\phi_2} \phi[\cos(\phi)P]^{10}\, d\phi}{\int_{\phi_1}^{\phi_2} [\cos(\phi)P]^{10}\, d\phi}, \tag{1}$$

where P is the precipitation and $\phi_1 = 0°$ and $\phi_2 = 20°\mathrm{N}$ are the latitude bounds for the integration. Therefore, the latitude and magnitude of the ITCZ were represented by the latitude and strength of the maximum precipitation over the north central Pacific. The ITCZ latitude was then used to classify the models into three categories. The 15 models with the southernmost meridional location of the ITCZ (orange bars in Fig. 1b) were classified as the normal ITCZ-type models ("normal type"); the 15 models with the northernmost meridional location of the ITCZ (green bars in Fig. 1b) were classified as the poleward (PW) ITCZ-type models ("PW type"); the remaining models were classified as "medium type" models (blue bars in Fig. 1b).

Note that the most obvious precipitation difference between the two model ensembles occurs during the boreal summer from June to September (JJAS; Fig. 2f). Therefore, in this study, the boreal summer season was defaulted as the months from June to September, unless it is particularly annotated.

3. Features of poleward ITCZ latitude bias that relate to ENSO phase locking

Based on the PLP index proposed by Liao et al. (2021), ENSO seasonal phase-locking simulation performance was evaluated for the 50 CMIP6 models (Fig. 1a). We further checked the connections between ENSO seasonal phase locking and the mean state components over the tropical Pacific. The correlation coefficients between the PLP index and climatological SST are weak (Fig. 1c). In contrast, the correlation coefficients between the PLP index and climatological precipitation are strong and significant (Fig. 1d). Specifically, we found significant positive and negative correlations over the northern tropical Pacific at 3°–7°N and 10°–14°N, 160°–240°E, respectively, which lie south and north of the observed Pacific ITCZ, respectively. Thus, it appears that there are strong connections between the simulation of the mean ITCZ position and ENSO seasonal phase-locking performance in the CMIP6 models.

TABLE 1. CMIP6 models used in this study and the corresponding ENSO seasonality diagnoses. The names of the models, the associated institutions and countries, the numbers of winter-peaking and total El Niño events, the latitude of the ITCZ, and the classifications are shown. For all models, the first ensemble member of the historical experiment ("r1i1p1f1") was analyzed over the period 1870–2014.

Model name	Model center; country	Winter-peaking/total El Niño events	ITCZ lat	Classification
ACCESS-CM2	CSIRO-BOM; Australia	34/45	6.23	Normal
ACCESS-ESM1-5	CSIRO-BOM; Australia	29/47	6.88	Normal
BCC-CSM2-MR	BCC; China	21/60	7.55	Normal
CAS-ESM2-0	CAS; China	29/54	7.03	Normal
CMCC-CM2-HR4	CMCC; Italy	20/33	7.45	Normal
CMCC-CM2-SR5	CMCC; Italy	20/28	7.85	Normal
CMCC-ESM2	CMCC; Italy	21/30	7.68	Normal
FGOALS-f3-L	LASG; China	26/44	6.95	Normal
FGOALS-g3	LASG; China	42/46	6.32	Normal
FIO-ESM-2-0	FIO; China	25/33	7.85	Normal
KACE-1-0-G	NIMS-KMA; South Korea	30/41	6.78	Normal
KIOST-ESM	KIOST; South Korea	20/46	7.68	Normal
MIROC6	CCSR; Japan	13/26	7.25	Normal
NorESM2-MM	NCC; Norway	20/30	6.91	Normal
TaiESM1	AS-RCEC; China	37/40	7.38	Normal
AWI-CM-1-1-MR	AWI; Germany	16/43	8.56	Medium
CESM2-WACCM	NCAR; United States	28/37	8.04	Medium
CESM2	NCAR; United States	27/41	7.90	Medium
CanESM5	CCCMA; Canada	15/37	8.32	Medium
E3SM-1-0	LLNL; United States	22/34	8.28	Medium
E3SM-1-1-ECA	LLNL; United States	23/44	8.43	Medium
E3SM-1-1	LLNL; United States	22/44	8.45	Medium
EC-Earth3-AerChem	EC-Earth Consortium; EC	30/43	8.37	Medium
EC-Earth3-Veg-LR	EC-Earth Consortium; EC	31/42	8.30	Medium
EC-Earth3-Veg	EC-Earth Consortium; EC	21/35	8.28	Medium
EC-Earth3	EC-Earth Consortium; EC	25/42	8.29	Medium
GISS-E2-2-H	NASA; United States	16/39	8.86	Medium
INM-CM4-8	INM; Russia	16/34	8.57	Medium
INM-CM5-0	INM; Russia	23/37	8.48	Medium
IPSL-CM6A-LR-INCA	IPSL; France	19/45	8.12	Medium
IPSL-CM6A-LR	IPSL; France	14/40	8.07	Medium
MRI-ESM2-0	MRI; Japan	13/36	8.72	Medium
NorCPM1	NCC; Norway	15/38	7.98	Medium
NorESM2-LM	NCC; Norway	17/39	8.41	Medium
SAM0-UNICON	SNU; South Korea	31/38	8.56	Medium
AWI-ESM-1-1-LR	AWI; Germany	18/41	9.71	PW
BCC-ESM1	BCC; China	33/54	8.93	PW
CAM-CSM1-0	CAMS; China	20/44	9.41	PW
CESM2-FV2	NCAR; United States	27/43	8.97	PW
CESM2-WACCM-FV2	NCAR; United States	23/35	9.30	PW
GFDL-ESM4	GFDL; United States	25/41	9.00	PW
GISS-E2-1-G-CC	NASA; United States	5/37	8.96	PW
GISS-E2-1-G	NASA; United States	10/36	9.02	PW
GISS-E2-1-H	NASA; United States	8/27	9.49	PW
ICON-ESM-LR	MPI-M; Germany	10/40	9.50	PW
IPSL-CM5A2-INCA	IPSL; France	8/42	9.79	PW
MPI-ESM-1-2-HAM	MPI; Germany	12/32	10.27	PW
MPI-ESM1-2-HR	MPI; Germany	14/36	8.91	PW
MPI-ESM1-2-LR	MPI; Germany	17/35	9.20	PW
NESM3	NUIST; China	20/45	10.77	PW

To determine how the mean ITCZ position influences the simulation of ENSO phase locking, we calculated the meridional location of the ITCZ as the latitude of the maximum precipitation over the north central Pacific (section 2b). The models with an equatorward mean location of the ITCZ tend to simulate a higher PLP index, which represents stronger ENSO seasonal phase locking (Fig. 1b).

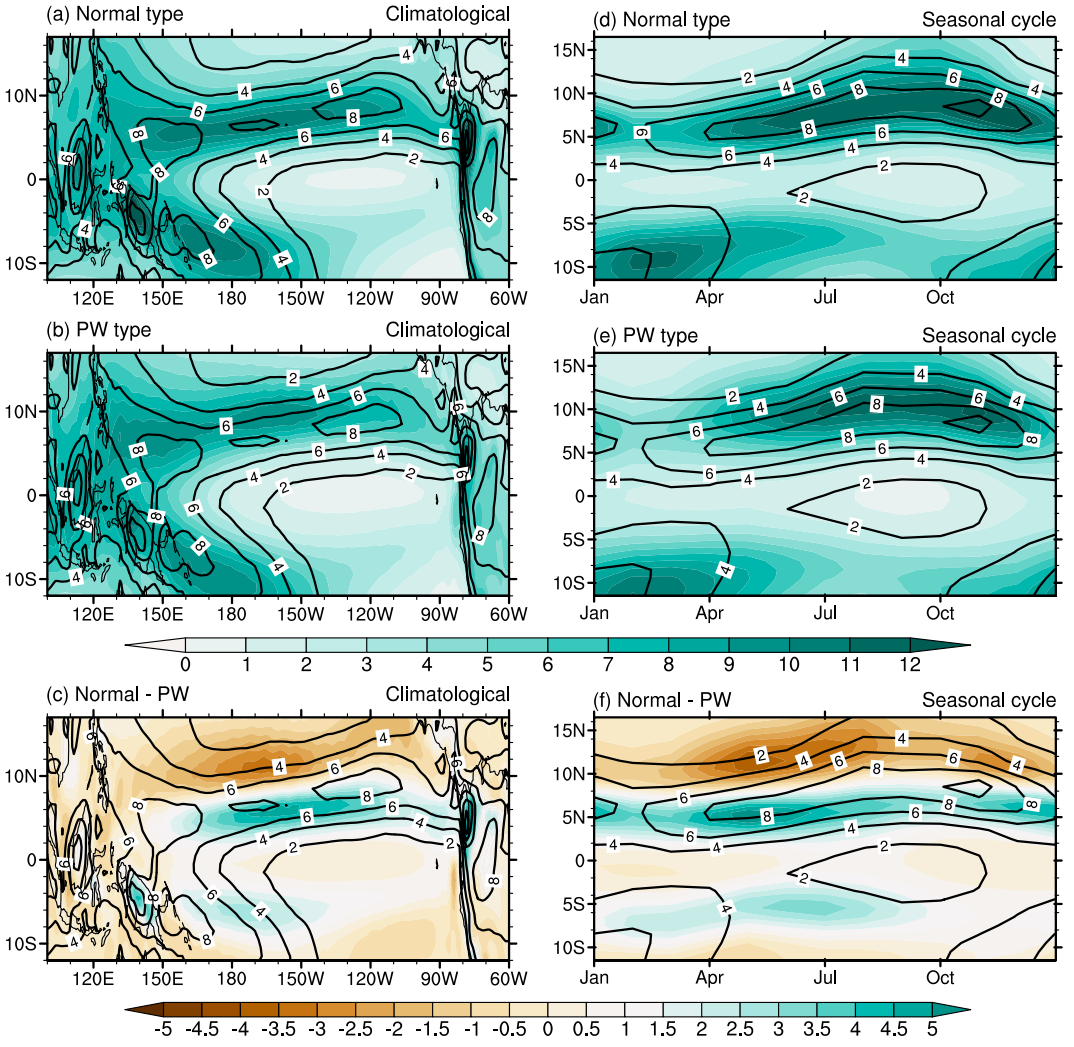

FIG. 2. Climatological and seasonal cycles of precipitation (mm day^{-1}) based on observations (GPCP) and ensemble means of the CMIP6 models. The ensemble mean climatological precipitation is based on (a) normal-type models, (b) PW-type models, and (c) normal-type models minus PW-type models. (d)–(f) Seasonal cycle of precipitation (mm day^{-1}) zonally averaged in 160°–240°E based on the same model ensembles as in (a)–(c). The observations are shown as contours.

We selected 15 models with the northernmost ITCZ position and 15 models with the southernmost ITCZ position (see section 2b; Table 1) and compared the ensemble differences to clarify the effects of the ITCZ latitude (Fig. 2). In reality, the climatological Pacific ITCZ lies at 4°–8°N in the north tropical Pacific, with a slight southwest–northeastward tilt. The maximum precipitation reaches 8 mm day^{-1}. Figure 2a shows that the spatial pattern of the mean precipitation of the southernmost ITCZ position model ensemble is much the same as in the observations, especially in the northern tropical Pacific near the ITCZ. The maximum precipitation of the ITCZ reaches 10 mm day^{-1}, which indicates that the southernmost ITCZ position is associated with the observation-liked but wetter spatial pattern of the Pacific ITCZ.

In comparison with the southernmost ITCZ position models, the models with the northernmost ITCZ position tended to simulate a poleward Pacific ITCZ (Fig. 2b). The maximum precipitation in the northernmost ITCZ position model ensemble lies at 7°–11°N in the north tropical Pacific, approximately 3° north of the observed ITCZ. The maximum precipitation value reached 9 mm day^{-1}, which is close to the strength of the southernmost ITCZ position model ensemble. Therefore, the most obvious difference between the two model ensembles is the meridional location of the ITCZ. This corresponds to our classification of the model ensemble with the southernmost ITCZ positions as the "normal type" and the northernmost ITCZ positions as the "PW type" (see section 2b).

To further illustrate the effect of the ITCZ mean meridional location, we used scatterplots to verify the connection between the ITCZ latitude and other indices. Based on the CMIP6 models, the correlation coefficient between the latitude of the

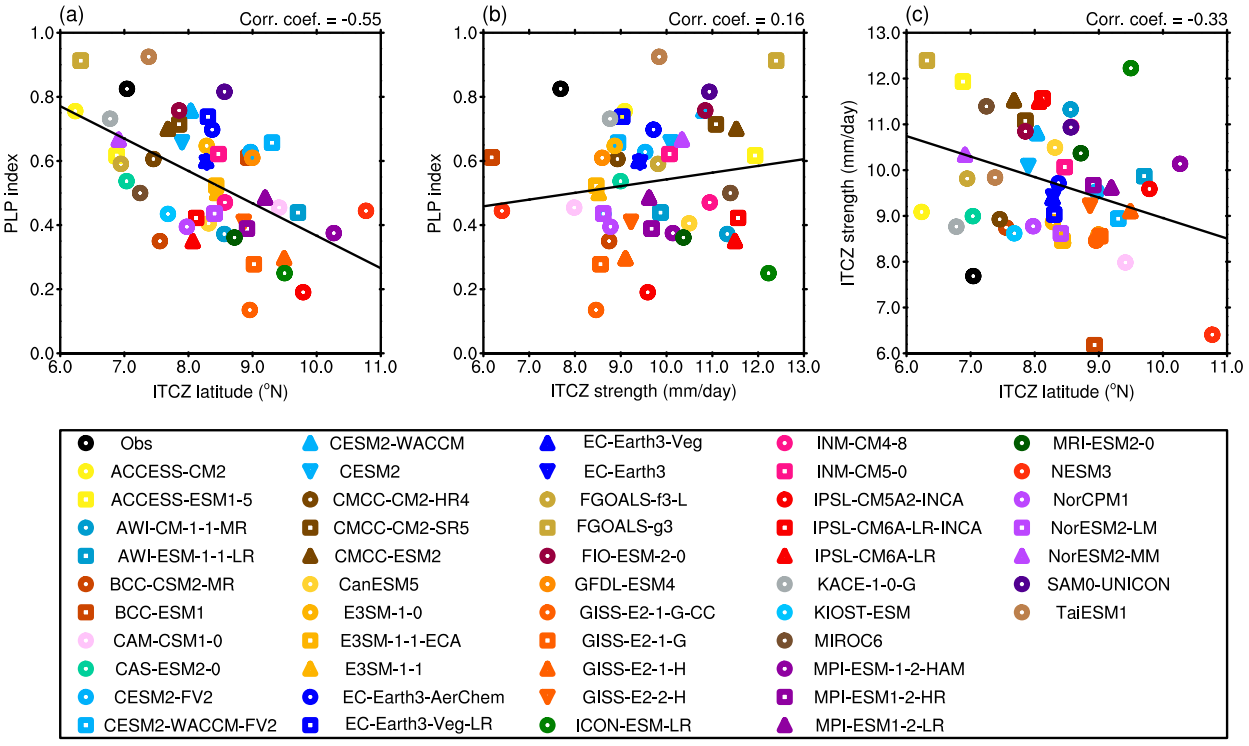

FIG. 3. Scatterplots of the PLP index against (a) the ITCZ latitude and (b) ITCZ strength based on observations and CMIP6 models. (c) Scatterplot of the ITCZ latitude against ITCZ strength. Black circles represent observations, and solid lines indicate regressions based on the simulated results. The correlation coefficients beyond 0.27 exceed the 95% confidence level.

ITCZ and the PLP index is −0.55, which indicates that the latitude of the ITCZ can explain about 30% of the ENSO seasonal phase-locking biases (Fig. 3a). This shows that the poleward ITCZ bias has significant connections with the ENSO seasonal phase-locking bias. In comparison, the correlation coefficient between the PLP index and the strength of the ITCZ is 0.16 (Fig. 3b), while the correlation coefficient between the strength and latitude of the ITCZ is −0.33 (Fig. 3c). These show that the ITCZ strength bias is less effective than the ENSO seasonal phase-locking bias, even though there are weak connections between the latitude and strength of the ITCZ biases.

Figure 2c shows the differences between the normal- and PW-type ITCZ models. The difference in the precipitation pattern is similar to the correlation map shown in Fig. 1d, with the most notable differences in the central Pacific at 160°–240°E; there are positive and negative precipitation values south and north of the observed ITCZ location, respectively. The absolute values of the differences reach 5 mm day^{-1}, which is almost half the maximum precipitation value. Although both types of models simulate a wetter ITCZ and stronger convection, the PW-type models simulate a stronger dry bias over the equatorial Pacific. Importantly, previous studies have suggested that the strength and meridional location of the ITCZ in models can influence the simulation of ENSO-related zonal wind responses, thereby modulating the evolution of ENSO events (Ham and Kug 2014a; Watanabe et al. 2011). However, it is impossible to determine how the poleward ITCZ latitude bias affects ENSO seasonal phase locking based solely on climatological analysis. As the phase-locking performance of ENSO is usually associated with the seasonal cycle (Chen and Jin 2022), further investigations of the poleward ITCZ latitude bias and the corresponding seasonal mechanisms are required.

4. Seasonality of the poleward ITCZ latitude bias and the mechanism that influences ENSO seasonal phase locking

a. Seasonal variation of the poleward ITCZ latitude bias

In the observations, the ITCZ showed clear seasonality, being weakest but most equatorward during the boreal spring and strongest and most poleward during the late boreal autumn (Fig. 2d). As the strength and meridional location of the ITCZ can modulate the ENSO-related surface wind response, they can further influence the simulation of ENSO events (Park et al. 2021). It is essential, therefore, to identify the seasonal occurrence of the most distinct ITCZ differences between the normal- and PW-type models to help determine the mechanisms that influence the simulation of ENSO seasonal phase locking.

Figures 2d and 2e show the ensemble means of the ITCZ seasonal cycle over the central Pacific (zonally averaged at 160°–240°E) in the normal- and PW-type models. Both ensembles simulated the broad seasonality of the ITCZ well.

There is also a clear difference between the two types of models; the latitudes of the ITCZ seasonal cycle in the normal-type models are almost the same as in the observations, whereas in the PW-type models, they move poleward. Indeed, in every season, the latitude of the ITCZ in the PW-type models is 2°–3° higher than that in the normal-type models. In addition to latitude, the biases when simulating the strength of the ITCZ also vary seasonally. Specifically, during the boreal spring, the maximum strength of the simulated precipitation is approximately 7 mm day^{-1} in both the normal- and PW-type models, which is close to the observations. However, during the boreal summer and autumn, this reaches 12 mm day^{-1}, which is approximately 3 mm day^{-1} higher than in the observations.

The most notable ITCZ differences between the normal- and PW-type model ensembles occur during the boreal summer, from June to September (Fig. 2f). The normal-type models simulate more precipitation near the equator (3°–7°N), while the PW-type models simulate more precipitation to the north (10°–14°N). This maximum precipitation difference exceeds 5 mm day^{-1}, which is almost half of the simulated precipitation strength in the ITCZ region. Therefore, in the PW-type models, the strongest bias over the equatorial Pacific occurs during the boreal summer.

This raises the question of why the ITCZ differences are concentrated in JJAS, even when the seasonal migration of the ITCZ in the normal- and PW-type models varies consistently. This can be explained by the combination of the seasonal cycle of ITCZ migration and strength. We evaluated ITCZ migration and strength based on the latitude and strength of the maximum precipitation over the north-central Pacific (see section 2b). Relative to the normal-type models, the PW-type models show a larger amplitude of ITCZ meridional migration (Fig. 4a). The maximum and minimum latitudes of the normal-type models reach 9.3° and 5.3°N, respectively. However, in the PW-type models, they reach 10.8° and 6.3°N, respectively. In addition, the northward ITCZ migration in the PW-type models is faster than in the normal-type models during the boreal spring and summer. Thus, the latitudinal difference between the two ensembles is larger between March and September but smaller from October to February.

In addition to latitude, the ITCZ strength of the two model ensembles in each season varies synchronously (Fig. 4b), with the ITCZ strength in the normal-type models always exceeding 1–2 mm day^{-1} of that in the PW-type models. Both the normal- and PW-type models simulated a strong positive bias in ITCZ strength from May to December. In particular, following the seasonality of the ITCZ, the simulated ITCZ strength reached a powerful level from June to December, with precipitation exceeding 11 mm day^{-1}. The clear difference between the normal- and PW-type models requires not only a large difference in the latitude of the ITCZ but also a sufficiently strong ITCZ. The most obvious precipitation difference between the two model ensembles occurs during the boreal summer, when the large ITCZ latitude difference coincides with the strong ITCZ period.

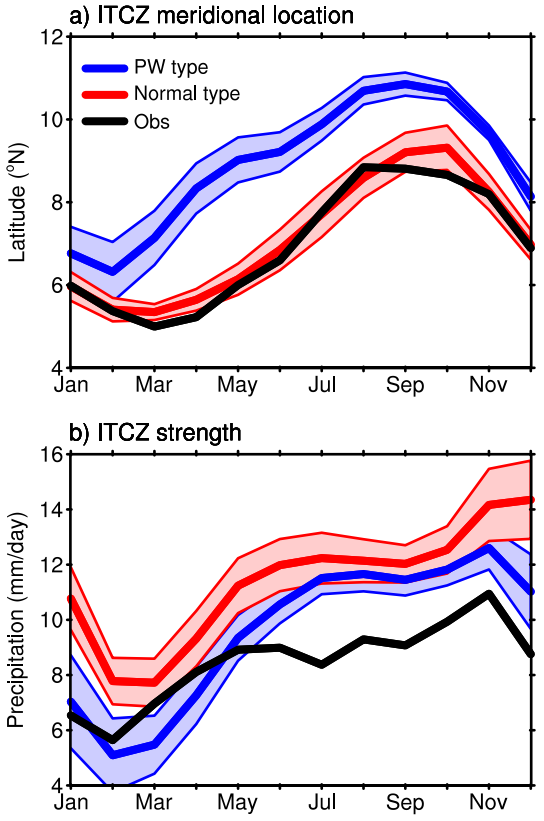

FIG. 4. Seasonal cycle of the (a) latitude and (b) strength of the ITCZ zonally averaged at 160°–240°E. Thick black, red, and blue lines represent the observations and ensemble means of the normal- and PW-type models, respectively. Light colors represent 0.5 times the intermodel SD.

b. Summer poleward ITCZ latitude bias and the corresponding ENSO-related zonal wind response

Studies suggested that the ITCZ is important to the development of ENSO events (Ham and Kug 2014a; Watanabe et al. 2011). During ENSO events, strong SST anomalies appear in the central-eastern equatorial Pacific, with a symmetrical meridional distribution (Fig. 5a). Since SST anomalies redistribute SST and a convective threshold of 27.5°C over the tropical Pacific, atmospheric deep convection and the associated precipitation are also shifted. Specifically, the ITCZ over the tropical Pacific moves equatorward during El Niño events (Fig. 5d), therefore inducing a westerly surface wind anomaly over the central-western equatorial Pacific (Fig. 5g). However, during La Niña events, the poleward movement of the ITCZ induces an easterly surface wind anomaly as a consequence.

Figures 5a and 5b show the spatial pattern of the ENSO-related summer SST anomalies in the normal- and PW-type models based on regressing the SST anomaly during JJAS onto the synchronous Niño-3 index. Both models show SST anomaly patterns that are similar to the observations. As the maximum difference reached 0.2, the differences between the two ensembles were negligible relative to the intensity of the ENSO events.

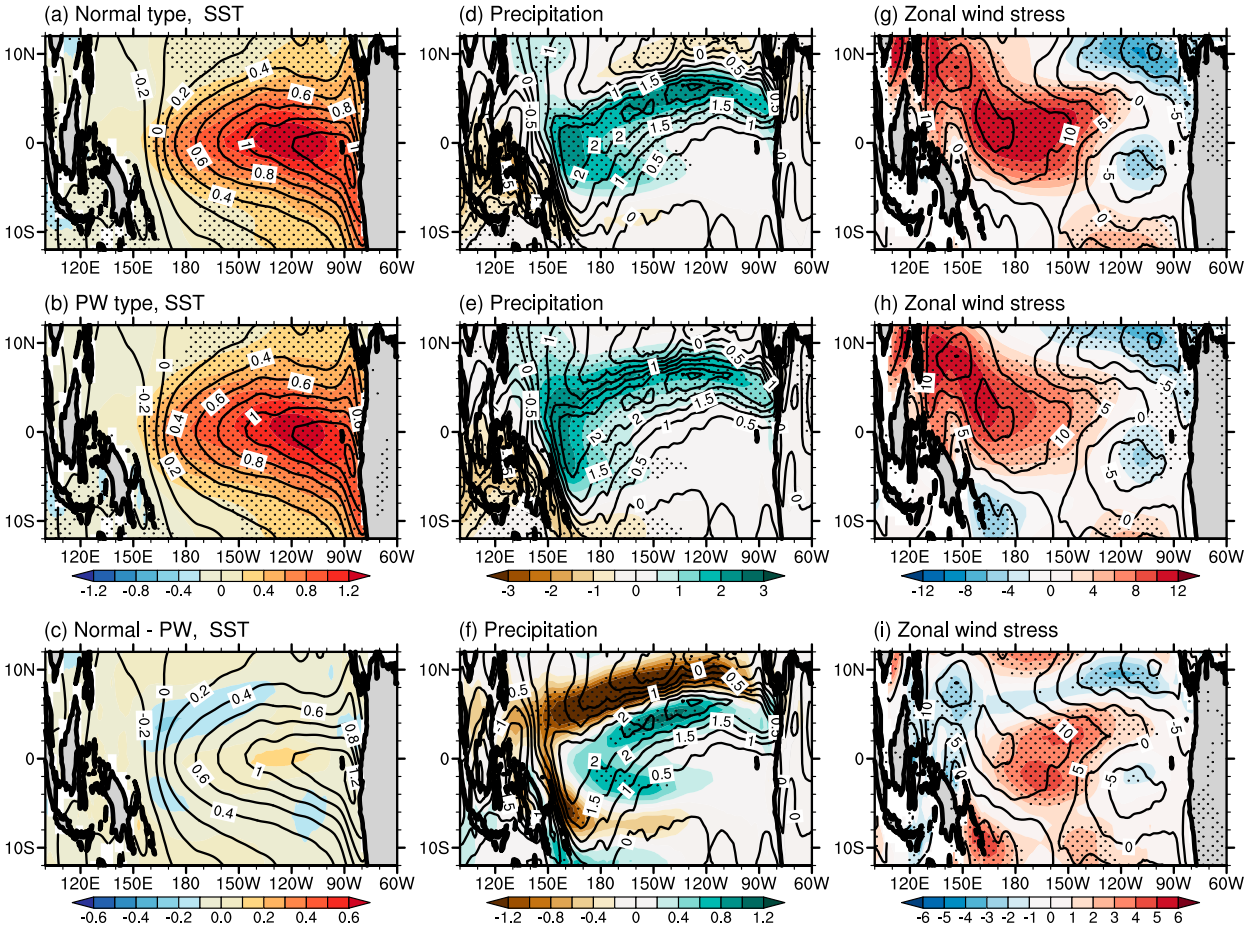

FIG. 5. SST, precipitation, and zonal wind stress anomalies regressed on the Niño-3 index during the boreal summer (June–September): ensemble means of the SST anomaly regressed on the Niño-3 index based on the (a) normal-type models, (b) PW-type models, and (c) normal-type models minus the PW-type models. (d)–(f) and (g)–(i) As in (a)–(c), but for the precipitation (mm day^{-1} °C^{-1}) and zonal wind stress (10^{-3} N m^{-2} °C) anomalies, respectively. The observations are shown by contours. Stippling in the top and middle rows represents where the ensemble means of the models exceed the intermodel SD; stippling in the bottom row represents where the differences between the two ensembles are statistically significant at the 95% confidence level.

As compared with the SST anomalies, the difference in the modeled spatial patterns of the ENSO-related precipitation anomalies is very clear. The spatial pattern of the ENSO-related precipitation responses in the normal-type models is similar to that in the observations (Fig. 5d), and the regression map shows positive regression signals over the western equatorial Pacific and north of the eastern tropical Pacific. These signals are located south of the climatological ITCZ, indicating that the Pacific ITCZ expands equatorward and shrinks poleward in response to the positive and negative SST anomalies, respectively. Therefore, more and less precipitation occurs over the central-west equatorial Pacific during El Niño and La Niña events, respectively, with the maximum precipitation response exceeding 2 mm day^{-1} °C^{-1}, which is identical to the observations.

In the PW-type models, the strength of the ENSO-related precipitation responses is similar to that in the observations (Fig. 5e). However, relative to the normal-type models, the ENSO-related precipitation anomaly moves north and westward. Therefore, the ENSO-related precipitation anomaly over the equator in the PW-type models is much weaker (Fig. 5f). The greatest differences occur over the central equatorial Pacific, with magnitudes exceeding 1.2 mm day^{-1} °C^{-1}, which is over half the strength of that in the observations and the models.

In tropical areas, strong precipitation is typically associated with deep atmospheric convection. During El Niño and La Niña events, in response to the precipitation anomaly and the associated deep convection anomaly over the equator, a westerly and easterly surface wind anomaly is generated over the central-western tropical Pacific, respectively. Both the normal- and PW-type models simulate significant surface wind stress anomalies that respond to ENSO events over the central-western tropical Pacific (Figs. 5g,h). However, since the ENSO-related precipitation anomaly over the equator is much weaker in the PW-type models during the boreal summer, the ENSO-related surface zonal wind stress anomaly is also much weaker. The most notable difference between the

two ensembles lies in the central equatorial Pacific (5°S–5°N, 160°–230°E; Fig. 5i). Here, the magnitude of the difference reaches 5×10^{-3} N m^{-2} °C, which is nearly half of the magnitude of the ENSO-related zonal wind stress responses in the normal models and observations. Therefore, during the boreal summer of El Niño and La Niña events, the PW-type models tend to simulate weaker westerly and easterly surface wind anomalies, respectively. The weak biases of the surface wind anomaly weaken the strength of the Bjerknes feedback in the boreal summer, thereby disturbing the development of ENSO in the PW-type models.

c. *Mechanism that influences the ENSO seasonal phase locking*

To shed further light on the mechanism that affects the simulation of ENSO seasonal phase locking, we checked the seasonality of ENSO-related surface wind responses in both model ensembles and observations (Fig. 6a). The ENSO-related wind anomaly was averaged in the region 5°S–5°N, 160°–230°E, where the greatest difference between the two ensembles is located. The ENSO-related surface wind response is weakest in March and strongest in October, which strictly follows the seasonal changing of the ITCZ (Fig. 4). The maximum and minimum ENSO-related surface wind stress responses exceeded 12×10^{-3} N m^{-2} °C and approximately 4×10^{-3} N m^{-2} °C, respectively.

The zonal wind anomaly that responds to the SST anomaly of ENSO is an essential step in the Bjerknes feedback that controls the development of ENSO events (Bjerknes 1969). The positive and negative SST anomalies of El Niño and La Niña events trigger westerly and easterly surface wind anomalies, which lead to the deepening and shoaling of the thermocline in the eastern tropical Pacific, respectively. This deepening and shoaling of the thermocline amplify the local SST anomaly, thereby supporting the continuing development of ENSO events. Therefore, following the seasonality of the ENSO-related surface wind stress response, the Bjerknes feedback is stronger during the boreal summer and autumn but weaker during the boreal spring.

During the boreal spring, the ENSO-related surface wind responses in both of the model types are approximately the same as in the observations (Fig. 6a). However, a large difference between the two types of models appears during the boreal summer. Similar to the observations, the ENSO-related surface wind response in the normal-type models increases rapidly. Although weaker than in the observations, the strength of the ENSO-related surface wind response during the boreal summer is approximately 2 times that in the boreal spring. However, in the PW-type models, the ENSO-related surface wind response is as weak as that in the boreal spring.

As the ENSO-related surface wind response differs significantly between the normal- and PW-type models during the boreal summer, the ENSO-related thermocline anomalies also differ. By regressing the thermocline depth anomaly onto the boreal summer Niño-3 index, we determined how the strength of the ENSO-related surface wind response affects the thermocline depth in each model type. Previous studies

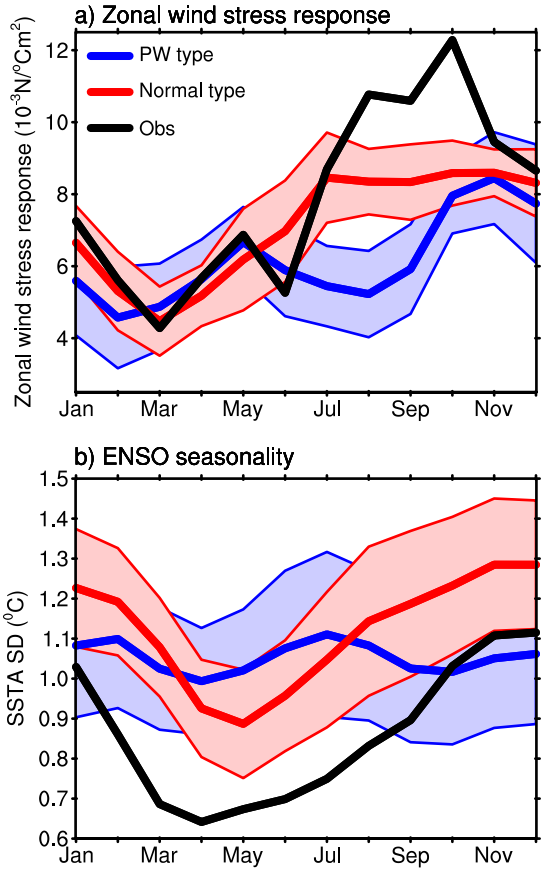

FIG. 6. ENSO-related zonal wind response and ENSO seasonality: (a) Zonal wind stress anomalies regressed onto the synchronous Niño-3 index in each calendar month for observations (black) and the ensemble means of normal- (red) and PW-type (blue) models. The zonal wind stress anomalies are averaged in the region 5°S–5°N, 160°–230°E. (b) SD of the Niño-3 SST anomalies (°C) for observations (black) and the ensemble means of normal- (red) and PW-type (blue) models. Shaded areas represent 0.5 times the intermodel SD.

have suggested that zonal wind anomalies over the central-western Pacific can trigger eastward-propagating Kelvin waves at the equator (Suarez and Schopf 1988). Notably, it takes approximately 3 months for Kelvin waves to propagate to the eastern Pacific (EP) and change the thermocline depth locally (Battisti 1989; Suarez and Schopf 1988). During the boreal summer, the thermocline anomalies that respond to ENSO events are similar in the two model ensembles (Figs. 7a–c), which can be attributed to the similar strength of the ENSO-related surface wind response in the preceding spring.

In the subsequent autumn, the thermocline anomalies that respond to ENSO events are enhanced in the normal-type models but remain largely unchanged in the PW-type models (Figs. 7d,e). The unchanged thermocline response in the PW-type models can be attributed to the weak ENSO-related zonal wind response during the boreal summer. The enhanced thermocline anomaly in the normal-type models further influences the upwelling of cold water from the deep ocean layer,

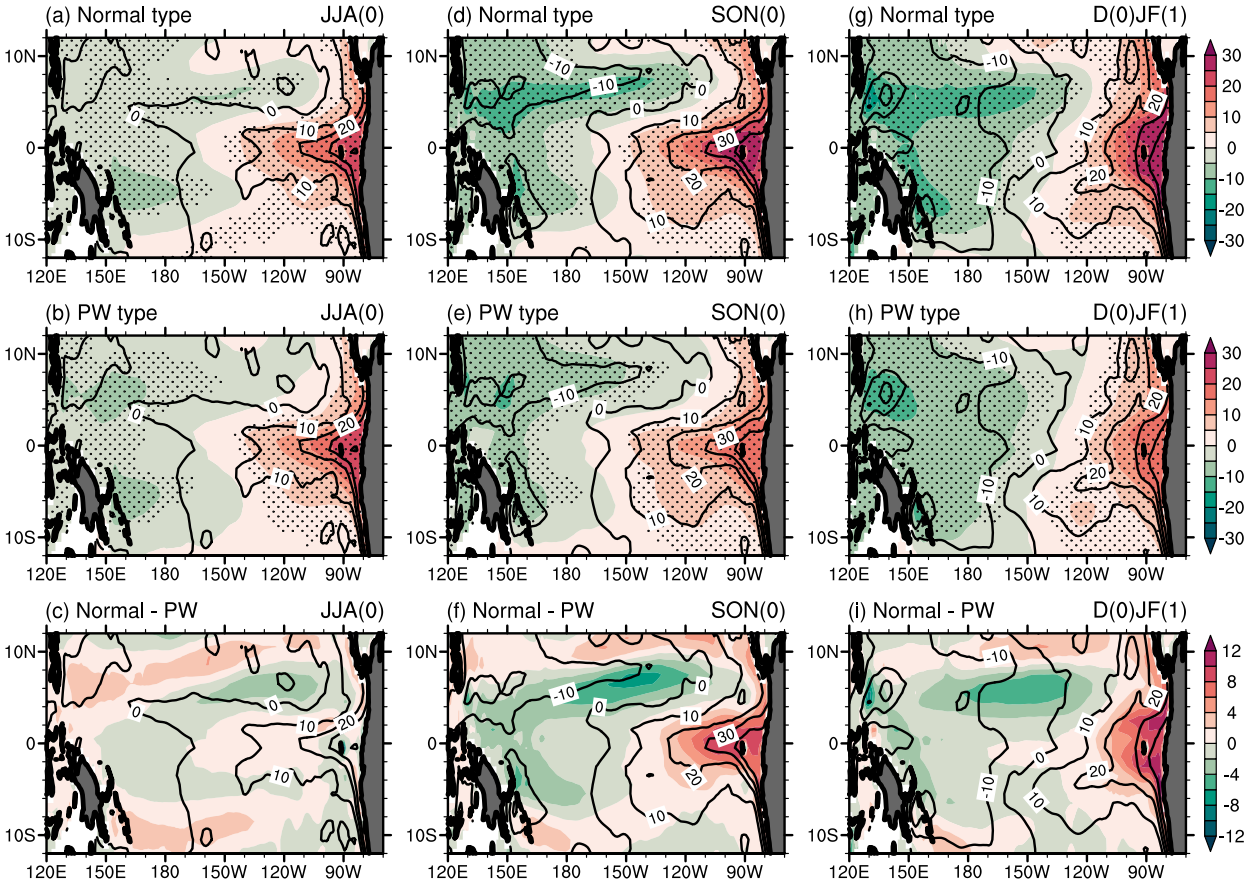

FIG. 7. Thermocline anomalies (m) during different seasons regressed onto the June–September Niño-3 index: Ensemble means of the thermocline anomaly during the boreal summer [June–August (JJA)] regressed onto the JJAS Niño-3 index based on (a) normal-type models, (b) PW-type models, and (c) normal-type models minus PW-type models. Year 0 indicates the same year with the JJAS Niño-3 index, and year 1 indicates the subsequent year. (d)–(f) and (g)–(i) As in (a)–(c), but for the thermocline anomaly during the boreal autumn [September–November (SON)] and boreal winter [December–February (DJF)], respectively. The observations are shown as contours. Stippling in the top and middle rows represents points where the ensemble means of the models exceed the intermodel SD.

thus favoring the growth of the SST anomaly. In the PW-type models, the unchanged thermocline anomaly cannot maintain the development of SST anomalies in the eastern tropical Pacific. Consequently, the development of ENSO events is stranded or even retrogressed in the PW-type models. A weaker autumn SST anomaly triggers a weaker zonal wind anomaly. Thus, the thermocline anomaly and the corresponding SST anomaly in the PW-type models during the boreal winter are also weaker than those in the normal-type models (Figs. 7g–i).

Jin et al. (2006) proposed the Bjerknes stability index, which decomposed the ENSO-related process into several aspects. They pointed out that, in addition to the thermocline anomaly, the zonal velocity anomaly in the mixed layer is also important to the evolution of ENSO. As the deepened thermocline cuts down the influence of the cold water from the deep ocean layer, which is called the thermocline feedback, the zonal current can also affect the SST through the horizontal heat advection called the zonal advection feedback. The westerly and easterly surface wind anomalies during El Niño and La Niña events lead eastward and westward seawater currents, respectively. Since the sea surface layer temperature in the western tropical Pacific is much higher than in the eastern tropical Pacific, the eastward and westward tropical currents amplify the warm and cold SST anomalies in the eastern tropical Pacific, respectively, through the horizontal heat advection (An et al. 1999; Picaut et al. 1997).

Unlike the thermocline responses, the zonal current responds faster to the ENSO-related surface wind anomaly. During the boreal summer, the strong ENSO-related surface wind anomalies in the observation and the normal-type models induce robust zonal current anomalies in the tropical Pacific (Fig. 8a). Therefore, they amplify the SST anomalies in the following autumn, triggering stronger ENSO-related surface wind anomalies and maintaining the growth of the ENSO events (Fig. 8d). However, since the ENSO-related surface wind anomalies in the PW-type models are relatively weak, the ENSO-related zonal current anomalies are also much weaker than in the normal-type models (Figs. 8a–c). The weaker zonal current anomalies cannot maintain the

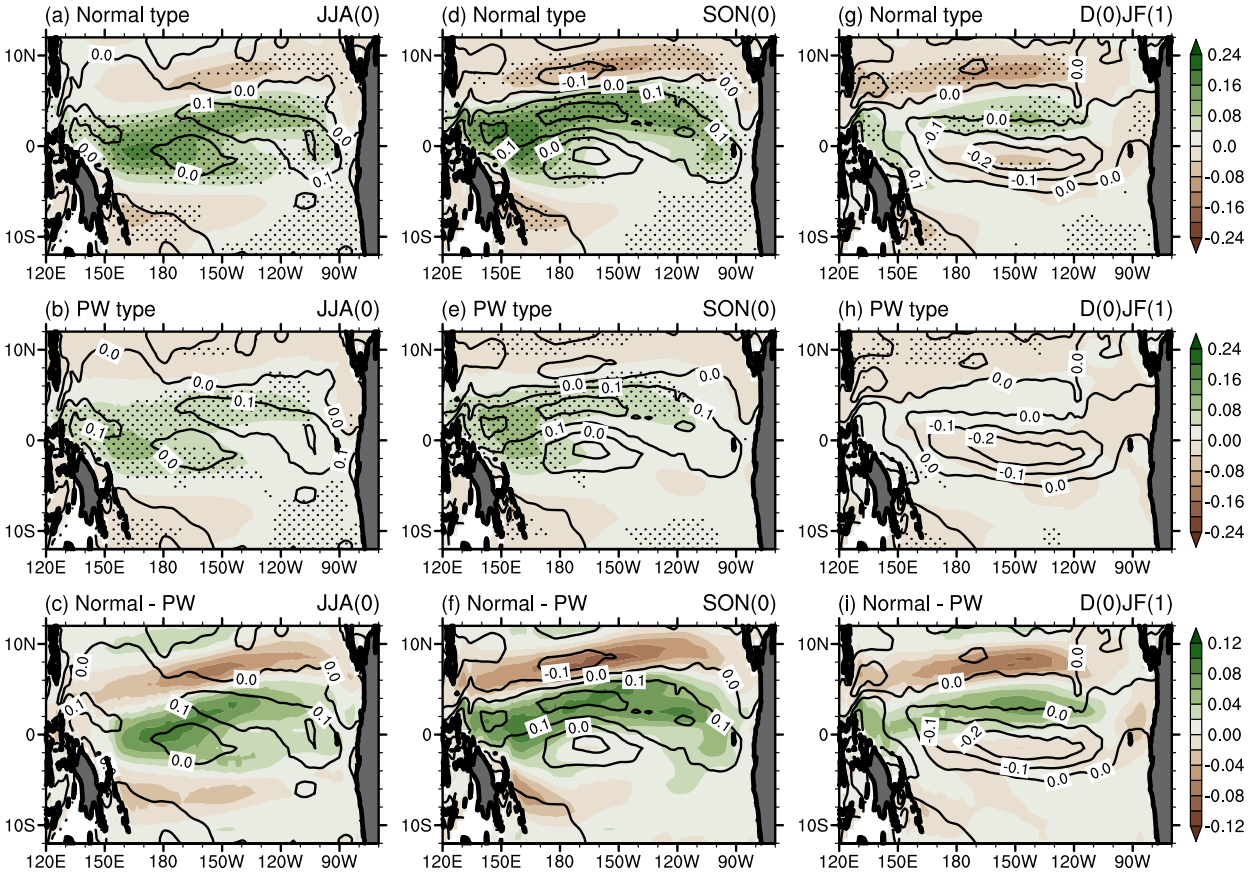

FIG. 8. As in Fig. 7, but for the mean seawater zonal velocity (m s^{-1}) in the mixed layer.

development of SST anomalies in the eastern tropical Pacific, thereby impeding the development of ENSO events in the following seasons.

Therefore, in the observations and the normal-type models, ENSO develops rapidly during the boreal summer and autumn but decays during the boreal spring, when the weak ENSO-related zonal wind response limits the Bjerknes feedback. Thus, winter-peaking ENSO events are favored. In the PW-type models, with the extremely weak ENSO-related zonal wind response during the boreal summer, ENSO events may stop growing or even abort, thereby disturbing the simulation of ENSO seasonal phase locking.

During the boreal autumn and winter, the SD of the Niño-3 index in the PW-type models is relatively low (Fig. 6b), indicating that the ENSO events in these models stopped growing and tended to peak out of the winter season. However, the seasonal variation of the Niño-3 SD in the normal-type models is identical to that in the observations, which indicates that a realistic simulation of ITCZ latitude is beneficial to the simulation of ENSO seasonal phase locking.

Note that in climate models, the poleward ITCZ latitude bias can be partly attributed to the spatial pattern of the SST bias (Zhou et al. 2020), while the tropical Pacific SST bias during the boreal summer is also recognized as an important factor that leads to the bias of ENSO seasonal phase locking (Ham et al. 2012; Kim et al. 2014). In addition, the bias in the simulated ITCZ resulted from multiple aspects, such as aerosol, cloud microphysics, atmospheric convection and large-scale circulation, and upper ocean temperature and circulation (Zhang et al. 2021), which may also lead to the ENSO seasonal phase-locking bias through certain physical processes. It is important to verify whether the poleward ITCZ latitude bias is a direct driver of the ENSO phase-locking bias or just an incidental phenomenon caused by other mechanisms. Our study proposed that the poleward ITCZ latitude bias weakens the ENSO-related zonal wind response during the boreal summer, thus affecting the simulation of ENSO seasonal phase locking. As the ENSO-related zonal wind response is recognized as an important factor that leads to the ENSO seasonal phase locking, it is also the key process that bonds the latitude of the ITCZ and ENSO phase locking. Therefore, the latitude of the ITCZ is a direct driver of the ENSO seasonal phase locking, as long as we verify that the latitude of the ITCZ can affect the ENSO-related zonal wind response independently.

Previous studies suggested that there are two main sources for the surface wind anomalies in the tropical Pacific: the SST gradient anomaly (Lindzen and Nigam 1987) and the deep convection anomaly (Gill 1980). The former is usually related to the spatial pattern of the SST, while the latter is usually associated with the location and strength of the ITCZ. Similarly,

the ENSO-related zonal wind response is also affected by these two aspects. Figures 9a and 9b show that both the latitude of the ITCZ and the SST in the central tropical Pacific Ocean can affect the strength of the ENSO-related zonal wind response during the boreal summer. However, after removing the influence of the central tropical Pacific SST on precipitation through linear regression, the connection between the latitude of the ITCZ and the ENSO-related zonal wind response is still significant (Fig. 9c). This shows that the ITCZ latitude bias can independently change the ENSO-related zonal wind response during the boreal summer. Therefore, it verifies that the poleward ITCZ latitude bias is a direct driver that leads to the ENSO seasonal phase-locking bias.

5. Discussion and conclusions

We evaluated the ability of 50 CMIP6 models to simulate ENSO phase locking and its connections with mean state components over the tropical Pacific. We found that the climatological latitude of the ITCZ can influence ENSO seasonal phase-locking simulation performance. The models with ITCZ latitudes similar to observations tend to simulate better ENSO seasonal phase locking, whereas the models with a poleward ITCZ latitude bias tend to simulate more ENSO events that peak out of the winter season. The contributions of the poleward ITCZ latitude bias to the ENSO phase-locking bias were also evaluated, yielding a correlation coefficient of −0.55, which corresponds to approximately 30% of the explained variance of the ENSO phase-locking bias. We named the former models the "normal type" and the latter the "PW type." As compared with observations and normal-type models, the PW-type models simulate a strong dry bias over the equatorial Pacific. The latitude of the ITCZ in the PW-type models is consistently 2°–3° higher than that in the normal-type models; however, the most notable differences in precipitation between the two model ensembles occur during the boreal summer, which is due to the combined effect of the seasonal change in ITCZ latitude and strength.

The mechanism that influences the simulation of ENSO seasonal phase locking in the CMIP6 models is summarized schematically in Fig. 10. In observations and the normal-type models, the strength of the Bjerknes feedback is stronger during the boreal summer and autumn but weaker during the boreal spring. Therefore, the seasonality of the Bjerknes feedback strength favors winter-peaking ENSO events. However, in the PW-type models, the poleward ITCZ latitude bias disturbs the seasonality of the Bjerknes feedback. That is, during the boreal summer, the poleward ITCZ latitude bias impedes the meridional movement of the ENSO-related ITCZ. The precipitation and convection anomalies that respond to ENSO events are also restrained over the equator. Following the convection bias, the zonal wind anomaly that responds to ENSO events is also weaker in the PW-type models during the boreal summer. The weaker zonal wind anomalies trigger weaker eastern tropical Pacific thermocline anomalies and zonal current anomalies during the boreal autumn, which is incapable of sustaining the further development of ENSO-related SST anomalies. Therefore, the ENSO events in PW-type models are restrained during the boreal summer and autumn and tend to peak out of the winter season.

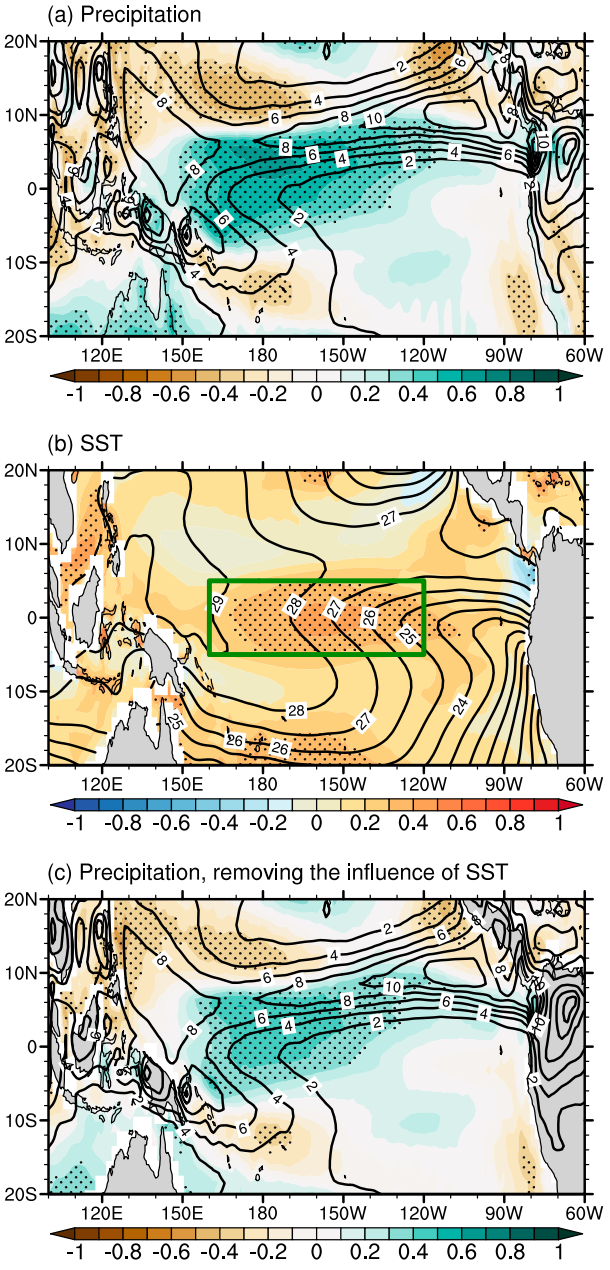

FIG. 9. Correlation coefficients (shading) between the ENSO-related zonal wind response and (a) precipitation and (b) SST during the boreal summer. The ENSO-related zonal wind response is calculated by regressing the zonal wind stress anomalies (averaged in the region 5°S–5°N, 160°–230°E) onto the synchronous Niño-3 index. (c) As in (a), but the impact of the tropical SST on the precipitation has been excluded by removing the linear regression with respect to the SST averaged in 5°S–5°N, 160°–240°E (green square in Fig. 9b). The observed climatological SST and precipitation are shown as contours. Stippling represents the regions where the correlation is statistically significant at the 95% confidence level.

Note that the model MAM-UA-1-0 is removed from the analysis. This model simulates the southernmost location of the mean meridional ITCZ location. However, the strength of the ITCZ is too weak to modulate the evolution of ENSO

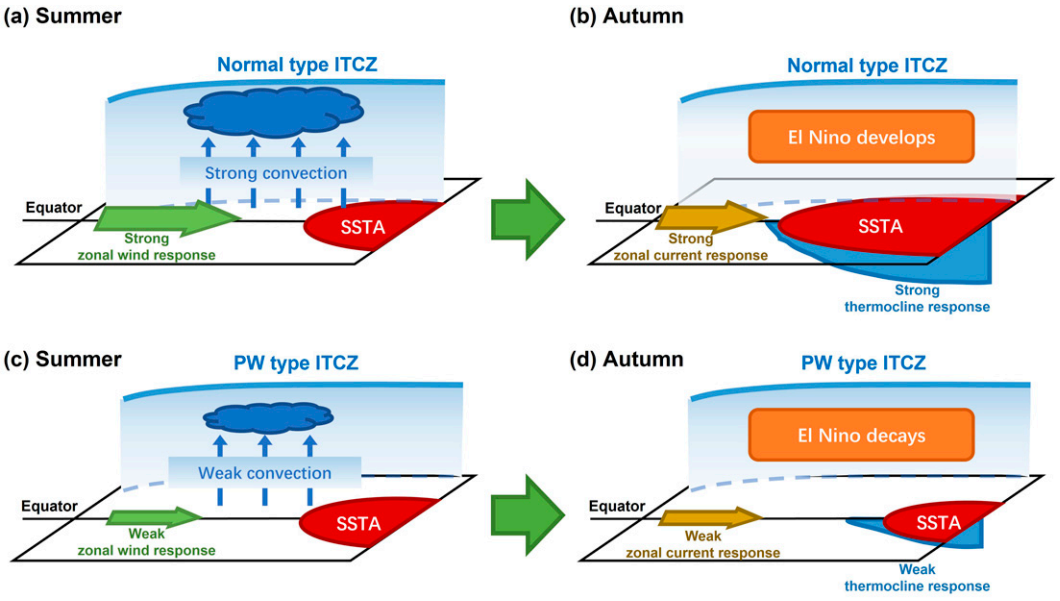

FIG. 10. Schematic diagram of the ENSO seasonal phase-locking bias induced by the poleward ITCZ latitude bias.

events. Therefore, the ENSO seasonal phase-locking bias in MAM-UA-1-0 is mainly affected by other background biases, such as the zonal SST gradient bias and thermocline bias (Ham et al. 2012; Wengel et al. 2018; Zhu et al. 2015). In future studies, we wish to investigate the ENSO seasonal phase locking in MCM-UA-1-0.

This study highlights the importance of the latitude of the ITCZ and provides a basis for the future development of climate models. In this study, the ENSO seasonal phase-locking simulation performance was evaluated by using El Niño events based on the Niño-3 index. We also examined the connections between the ITCZ and ENSO seasonal phase-locking performance for El Niño events based on the Niño-3.4 index and through La Niña events based on the Niño-3 index. We identified significant connections, with correlation coefficients reaching 0.42 and 0.52, respectively. The lower correlation coefficient based on the Niño-3.4 index may be due to the better phase-locking performance of the Niño-3.4 SST anomaly. The SST anomaly in the Niño-3 region usually represents EP El Niño events, while the SST anomaly in the Niño-3.4 region usually contains information on CP El Niño events (Ashok et al. 2007; Kug et al. 2009). Further investigations on the possible connections between the simulated ITCZ and EP/CP El Niño events and their associated mechanisms are still needed. Moreover, there are uneven connections between the ITCZ and ENSO seasonal phase-locking performance based on El Niño and La Niña events (Choi et al. 2015) that also require further investigation.

In addition to the poleward ITCZ latitude bias, there is also a significant bias when simulating the SPCZ. Both types of models simulated a strong and westerly extended SPCZ. The SPCZ in the boreal winter and spring is crucial to ENSO phase locking because it can induce the southward movement of ENSO-related zonal wind anomalies and generate winter-peaked ENSO events (McGregor et al. 2012). However, we found no significant correlations between the PLP index and climatological precipitation in the SPCZ region (Fig. 1d). This may be due to the smoothed signals obtained from climatological analyses. Further studies on the connections between the SPCZ and ENSO seasonal phase locking in CMIP6 should nevertheless focus on the winter and spring seasons.

Because we mainly focused on the influence of the ITCZ on ENSO seasonal phase locking, the connections between the simulated poleward ITCZ latitude bias and other component biases in the tropical Pacific require further attention, especially those connections with SST bias (Samanta et al. 2019). Indeed, the strength and location of the ITCZ are strongly related to SST. However, in climate models, the bias in simulating ITCZ results in a complex chain of interactions, including aerosol, cloud microphysics, atmospheric convection and large-scale circulation, and upper ocean temperature and circulation (Hu et al. 2022; Mamalakis et al. 2021; Samuels et al. 2021; Zhang et al. 2021, 2007). Notably, previous studies have suggested that multiple component biases can affect the simulation performance of ENSO phase locking, such as the excessive summer zonal SST gradient (Ham et al. 2012), the unrealistic seasonal cycle of the zonal SST gradient (Liao et al. 2021), the double ITCZ problem (Zheng and Yu 2007), shortwave feedback bias (Bellenger et al. 2014), an incorrect mean current (Stein et al. 2010), and an overly shallow thermocline depth (Wengel et al. 2018; Zhu et al. 2015). Thus, the combined effects of these simulation biases require further investigation in future studies.

Acknowledgments. This research was funded by the National Natural Science Foundation of China (42022042 and 41821004), the Basic Scientific Fund for National Public Research Institute of China (Shu-Xingbei Young Talent Program 2023S01), the CAS

Interdisciplinary Innovation Team (JCTD-2020-12), and the China–Korea Cooperation Project on Northwest Pacific Marine Ecosystem Simulation under Climate Change.

Data availability statement. All the data in this paper are publicly available online (SST: https://psl.noaa.gov/data/gridded/data.noaa.ersst.v5.html; GPCP: https://psl.noaa.gov/data/gridded/data.gpcp.html; GODAS: https://psl.noaa.gov/data/gridded/data.godas.html; the CMIP6 model dataset: https://esgf-node.llnl.gov/search/cmip6/).

REFERENCES

Abellán, E., and S. McGregor, 2016: The role of the southward wind shift in both, the seasonal synchronization and duration of ENSO events. *Climate Dyn.*, **47**, 509–527, https://doi.org/10.1007/s00382-015-2853-1.

——, ——, and M. H. England, 2017: Analysis of the southward wind shift of ENSO in CMIP5 models. *J. Climate*, **30**, 2415–2435, https://doi.org/10.1175/JCLI-D-16-0326.1.

Adam, O., 2018: Zonally varying ITCZs in a Matsuno–Gill-type model with an idealized Bjerknes feedback. *J. Adv. Model. Earth Syst.*, **10**, 1304–1318, https://doi.org/10.1029/2017MS001183.

——, T. Bischoff, and T. Schneider, 2016: Seasonal and interannual variations of the energy flux equator and ITCZ. Part I: Zonally averaged ITCZ position. *J. Climate*, **29**, 3219–3230, https://doi.org/10.1175/JCLI-D-15-0512.1.

Adler, R. F., and Coauthors, 2018: The Global Precipitation Climatology Project (GPCP) monthly analysis (new version 2.3) and a review of 2017 global precipitation. *Atmosphere*, **9**, 138, https://doi.org/10.3390/atmos9040138.

An, S.-I., F.-F. Jin, and I.-S. Kang, 1999: The role of zonal advection feedback in phase transition and growth of ENSO in the Cane–Zebiak model. *J. Meteor. Soc. Japan*, **77**, 1151–1160, https://doi.org/10.2151/jmsj1965.77.6_1151.

Ashok, K., S. K. Behera, S. A. Rao, H. Weng, and T. Yamagata, 2007: El Niño Modoki and its possible teleconnection. *J. Geophys. Res.*, **112**, C11007, https://doi.org/10.1029/2006JC003798.

Battisti, D. S., 1989: On the role of off-equatorial oceanic Rossby waves during ENSO. *J. Phys. Oceanogr.*, **19**, 551–560, https://doi.org/10.1175/1520-0485(1989)019<0551:OTROOE>2.0.CO;2.

Behringer, D., and Y. Xue, 2004: Evaluation of the Global Ocean Data Assimilation System at NECP: The Pacific Ocean. *Eighth Symp. on Integrated Observing and Assimilation Systems for Atmosphere, Oceans, and Land Surface*, Seattle, WA, Amer. Meteor. Soc., 2.3, https://ams.confex.com/ams/pdfpapers/70720.pdf.

Bellenger, H., É. Guilyardi, J. Leloup, M. Lengaigne, and J. Vialard, 2014: ENSO representation in climate models: From CMIP3 to CMIP5. *Climate Dyn.*, **42**, 1999–2018, https://doi.org/10.1007/s00382-013-1783-z.

Bjerknes, J., 1969: Atmospheric teleconnections from the equatorial Pacific. *Mon. Wea. Rev.*, **97**, 163–172, https://doi.org/10.1175/1520-0493(1969)097<0163:ATFTEP>2.3.CO;2.

Chen, H.-C., and F.-F. Jin, 2021: Simulations of ENSO phase-locking in CMIP5 and CMIP6. *J. Climate*, **34**, 5135–5149, https://doi.org/10.1175/JCLI-D-20-0874.1.

——, and ——, 2022: Dynamics of ENSO phase-locking and its biases in climate models. *Geophys. Res. Lett.*, **49**, e2021GL097603, https://doi.org/10.1029/2021GL097603.

Chen, X., H. Liao, X. Lei, Y. Bao, and Z. Song, 2019: Analysis of ENSO simulation biases in FIO-ESM version 1.0. *Climate Dyn.*, **53**, 6933–6946, https://doi.org/10.1007/s00382-019-04969-w.

Chiang, J. C. H., and D. J. Vimont, 2004: Analogous Pacific and Atlantic meridional modes of tropical atmosphere–ocean variability. *J. Climate*, **17**, 4143–4158, https://doi.org/10.1175/JCLI4953.1.

——, S. E. Zebiak, and M. A. Cane, 2001: Relative roles of elevated heating and surface temperature gradients in driving anomalous surface winds over tropical oceans. *J. Atmos. Sci.*, **58**, 1371–1394, https://doi.org/10.1175/1520-0469(2001)058<1371:RROEHA>2.0.CO;2.

Choi, K.-Y., G. A. Vecchi, and A. T. Wittenberg, 2015: Nonlinear zonal wind response to ENSO in the CMIP5 models: Roles of the zonal and meridional shift of the ITCZ/SPCZ and the simulated climatological precipitation. *J. Climate*, **28**, 8556–8573, https://doi.org/10.1175/JCLI-D-15-0211.1.

Deser, C., and J. M. Wallace, 1990: Large-scale atmospheric circulation features of warm and cold episodes in the tropical Pacific. *J. Climate*, **3**, 1254–1281, https://doi.org/10.1175/1520-0442(1990)003<1254:LSACFO>2.0.CO;2.

——, M. A. Alexander, S.-P. Xie, and A. S. Phillips, 2010: Sea surface temperature variability: Patterns and mechanisms. *Annu. Rev. Mar. Sci.*, **2**, 115–143, https://doi.org/10.1146/annurev-marine-120408-151453.

Dippe, T., J. F. Lübbecke, and R. J. Greatbatch, 2019: A comparison of the Atlantic and Pacific Bjerknes feedbacks: Seasonality, symmetry, and stationarity. *J. Geophys. Res. Oceans*, **124**, 2374–2403, https://doi.org/10.1029/2018JC014700.

Eyring, V., S. Bony, G. A. Meehl, C. A. Senior, B. Stevens, R. J. Stouffer, and K. E. Taylor, 2016: Overview of the Coupled Model Intercomparison Project phase 6 (CMIP6) experimental design and organization. *Geosci. Model Dev.*, **9**, 1937–1958, https://doi.org/10.5194/gmd-9-1937-2016.

Fang, X.-H., F. Zheng, Z.-Y. Liu, and J. Zhu, 2019: Decadal modulation of ENSO spring persistence barrier by thermal damping processes in the observation. *Geophys. Res. Lett.*, **46**, 6892–6899, https://doi.org/10.1029/2019GL082921.

Gill, A. E., 1980: Some simple solutions for heat-induced tropical circulation. *Quart. J. Roy. Meteor. Soc.*, **106**, 447–462, https://doi.org/10.1002/qj.49710644905.

Guilyardi, E., P. Delecluse, S. Gualdi, and A. Navarra, 2003: Mechanisms for ENSO phase change in a coupled GCM. *J. Climate*, **16**, 1141–1158, https://doi.org/10.1175/1520-0442(2003)16<1141:MFEPCI>2.0.CO;2.

Ham, Y.-G., and J.-S. Kug, 2014a: Effects of Pacific intertropical convergence zone precipitation bias on ENSO phase transition. *Environ. Res. Lett.*, **9**, 064008, https://doi.org/10.1088/1748-9326/9/6/064008.

——, and ——, 2014b: ENSO phase-locking to the boreal winter in CMIP3 and CMIP5 models. *Climate Dyn.*, **43**, 305–318, https://doi.org/10.1007/s00382-014-2064-1.

——, ——, D. Kim, Y.-H. Kim, and D.-H. Kim, 2012: What controls phase-locking of ENSO to boreal winter in coupled GCMs? *Climate Dyn.*, **40**, 1551–1568, https://doi.org/10.1007/s00382-012-1420-2.

Hu, Y., X. Wang, J.-J. Luo, D. Wang, H. Yan, C. Yuan, and X. Lin, 2022: Forecasts of MJO during DYNAMO in a coupled tropical channel model: Impact of planetary boundary layer schemes. *Atmosphere*, **13**, 666, https://doi.org/10.3390/atmos13050666.

Huang, B., Y. Xue, D. Zhang, A. Kumar, and M. J. McPhaden, 2010: The NCEP GODAS ocean analysis of the tropical

Pacific mixed layer heat budget on seasonal to interannual time scales. *J. Climate*, **23**, 4901–4925, https://doi.org/10.1175/2010JCLI3373.1.

——, and Coauthors, 2017: Extended Reconstructed Sea Surface Temperature, version 5 (ERSSTv5): Upgrades, validations, and intercomparisons. *J. Climate*, **30**, 8179–8205, https://doi.org/10.1175/JCLI-D-16-0836.1.

Jin, F.-F., 1997a: An equatorial ocean recharge paradigm for ENSO. Part I: Conceptual model. *J. Atmos. Sci.*, **54**, 811–829, https://doi.org/10.1175/1520-0469(1997)054<0811:AEORPF>2.0.CO;2.

——, 1997b: An equatorial ocean recharge paradigm for ENSO. Part II: A stripped-down coupled model. *J. Atmos. Sci.*, **54**, 830–847, https://doi.org/10.1175/1520-0469(1997)054<0830:AEORPF>2.0.CO;2.

——, S. T. Kim, and L. Bejarano, 2006: A coupled-stability index for ENSO. *Geophys. Res. Lett.*, **33**, L23708, https://doi.org/10.1029/2006GL027221.

Kim, S. T., W. Cai, F.-F. Jin, and J.-Y. Yu, 2014: ENSO stability in coupled climate models and its association with mean state. *Climate Dyn.*, **42**, 3313–3321, https://doi.org/10.1007/s00382-013-1833-6.

Kug, J.-S., F.-F. Jin, and S.-I. An, 2009: Two types of El Niño events: Cold tongue El Niño and warm pool El Niño. *J. Climate*, **22**, 1499–1515, https://doi.org/10.1175/2008JCLI2624.1.

Levine, A., and M. J. McPhaden, 2015: The annual cycle in ENSO growth rate as a cause of the spring predictability barrier. *Geophys. Res. Lett.*, **42**, 5034–5041, https://doi.org/10.1002/2015GL064309.

——, F. F. Jin, and M. J. McPhaden, 2016: Extreme noise–extreme El Niño: How state-dependent noise forcing creates El Niño–La Niña asymmetry. *J. Climate*, **29**, 5483–5499, https://doi.org/10.1175/JCLI-D-16-0091.1.

Li, T., and S. G. H. Philander, 1996: On the annual cycle of the eastern equatorial Pacific. *J. Climate*, **9**, 2986–2998, https://doi.org/10.1175/1520-0442(1996)009<2986:OTACOT>2.0.CO;2.

Liao, H., C. Wang, and Z. Song, 2021: ENSO phase-locking biases from the CMIP5 to CMIP6 models and a possible explanation. *Deep-Sea Res. II*, **189–190**, 104943, https://doi.org/10.1016/j.dsr2.2021.104943.

Lindsey, R., 2013: In watching for El Niño and La Niña, NOAA adapts to global warming. NOAA Climate Watch, https://www.climate.gov/news-features/understanding-climate/watching-el-niño-and-la-niña-noaa-adapts-global-warming.

Lindzen, R. S., and S. Nigam, 1987: On the role of sea surface temperature gradients in forcing low-level winds and convergence in the tropics. *J. Atmos. Sci.*, **44**, 2418–2436, https://doi.org/10.1175/1520-0469(1987)044<2418:OTROSS>2.0.CO;2.

Mamalakis, A., and Coauthors, 2021: Zonally contrasting shifts of the tropical rain belt in response to climate change. *Nat. Climate Change*, **11**, 143–151, https://doi.org/10.1038/s41558-020-00963-x.

McGregor, S., A. Timmermann, N. Schneider, M. F. Stuecker, and M. H. England, 2012: The effect of the South Pacific convergence zone on the termination of El Niño events and the meridional asymmetry of ENSO. *J. Climate*, **25**, 5566–5586, https://doi.org/10.1175/JCLI-D-11-00332.1.

——, N. Ramesh, P. Spence, M. H. England, M. J. McPhaden, and A. Santoso, 2013: Meridional movement of wind anomalies during ENSO events and their role in event termination. *Geophys. Res. Lett.*, **40**, 749–754, https://doi.org/10.1002/grl.50136.

Mitchell, T. P., and J. M. Wallace, 1992: The annual cycle in equatorial convection and sea surface temperature. *J. Climate*, **5**, 1140–1156, https://doi.org/10.1175/1520-0442(1992)005<1140:TACIEC>2.0.CO;2.

——, and ——, 1996: ENSO seasonality: 1950–78 versus 1979–92. *J. Climate*, **9**, 3149–3161, https://doi.org/10.1175/1520-0442(1996)009<3149:ESV>2.0.CO;2.

Neelin, J. D., F.-F. Jin, and H.-H. Syu, 2000: Variations in ENSO phase locking. *J. Climate*, **13**, 2570–2590, https://doi.org/10.1175/1520-0442(2000)013<2570:VIEPL>2.0.CO;2.

Park, J.-H., M.-K. Sung, Y.-M. Yang, J. Zhao, S.-I. An, and J.-S. Kug, 2021: Role of the climatological intertropical convergence zone in the seasonal footprinting mechanism of El Niño–Southern Oscillation. *J. Climate*, **34**, 5243–5256, https://doi.org/10.1175/JCLI-D-20-0809.1.

Philander, S. G. H., 1983: El Niño Southern Oscillation phenomena. *Nature*, **302**, 295–301, https://doi.org/10.1038/302295a0.

Picaut, J., F. Masia, and Y. du Penhoat, 1997: An advective–reflective conceptual model for the oscillatory nature of the ENSO. *Science*, **277**, 663–666, https://doi.org/10.1126/science.277.5326.663.

Rashid, H. A., and A. C. Hirst, 2016: Investigating the mechanisms of seasonal ENSO phase locking bias in the ACCESS coupled model. *Climate Dyn.*, **46**, 1075–1090, https://doi.org/10.1007/s00382-015-2633-y.

Samanta, D., K. B. Karnauskas, and N. F. Goodkin, 2019: Tropical Pacific SST and ITCZ biases in climate models: Double trouble for future rainfall projections? *Geophys. Res. Lett.*, **46**, 2242–2252, https://doi.org/10.1029/2018GL081363.

Samuels, M., O. Adam, and H. Gildor, 2021: A shallow thermocline bias in the southern tropical Pacific in CMIP5/6 models linked to double-ITCZ bias. *Geophys. Res. Lett.*, **48**, e2021GL093818, https://doi.org/10.1029/2021GL093818.

Si, W., H. Liu, X. Zhang, and M. Zhang, 2021: Double intertropical convergence zones in coupled ocean–atmosphere models: Progress in CMIP6. *Geophys. Res. Lett.*, **48**, e2021GL094779, https://doi.org/10.1029/2021GL094779.

Stein, K., N. Schneider, A. Timmermann, and F.-F. Jin, 2010: Seasonal synchronization of ENSO events in a linear stochastic model. *J. Climate*, **23**, 5629–5643, https://doi.org/10.1175/2010JCLI3292.1.

Suarez, M. J., and P. S. Schopf, 1988: A delayed action oscillator for ENSO. *J. Atmos. Sci.*, **45**, 3283–3287, https://doi.org/10.1175/1520-0469(1988)045<3283:ADAOFE>2.0.CO;2.

Tian, B., and X. Dong, 2020: The double-ITCZ bias in CMIP3, CMIP5, and CMIP6 models based on annual mean precipitation. *Geophys. Res. Lett.*, **47**, e2020GL087232, https://doi.org/10.1029/2020GL087232.

Wang, C., and J. Picaut, 2004: Understanding ENSO physics—A review. *Earth's Climate: The Ocean–Atmosphere Interaction*, *Geophys. Monogr.*, Vol. 147, Amer. Geophys. Union, 21–48.

Watanabe, M., M. Chikira, Y. Imada, and M. Kimoto, 2011: Convective control of ENSO simulated in MIROC. *J. Climate*, **24**, 543–562, https://doi.org/10.1175/2010JCLI3878.1.

Wengel, C., M. Latif, W. Park, J. Harlaß, and T. Bayr, 2018: Seasonal ENSO phase locking in the Kiel climate model: The importance of the equatorial cold sea surface temperature bias. *Climate Dyn.*, **50**, 901–919, https://doi.org/10.1007/s00382-017-3648-3.

Xie, S.-P., 1994: On the genesis of the equatorial annual cycle. *J. Climate*, **7**, 2008–2013, https://doi.org/10.1175/1520-0442(1994)007<2008:OTGOTE>2.0.CO;2.

——, and J. A. Carton, 2004: Tropical Atlantic variability: Patterns, mechanisms, and impacts. *Earth's Climate: The Ocean–Atmosphere Interaction*, *Geophys. Monogr.*, Vol. 147, Amer. Geophys. Union, 121–142.

——, Q. Peng, Y. Kamae, X.-T. Zheng, H. Tokinaga, and D. Wang, 2018: Eastern Pacific ITCZ dipole and ENSO diversity. *J. Climate*, **31**, 4449–4462, https://doi.org/10.1175/JCLI-D-17-0905.1.

Zhang, H., X. Ma, S. Zhao, and L. Kong, 2021: Advances in research on the ITCZ: Mean position, model bias, and anthropogenic aerosol influences. *J. Meteor. Res.*, **35**, 729–742, https://doi.org/10.1007/s13351-021-0203-2.

Zhang, X., W. Lin, and M. Zhang, 2007: Toward understanding the double intertropical convergence zone pathology in coupled ocean–atmosphere general circulation models. *J. Geophys. Res.*, **112**, D12102, https://doi.org/10.1029/2006JD007878.

Zheng, F., and J. Zhu, 2010: Spring predictability barrier of ENSO events from the perspective of an ensemble prediction system. *Global Planet. Change*, **72**, 108–117, https://doi.org/10.1016/j.gloplacha.2010.01.021.

Zheng, W., and Y. Yu, 2007: ENSO phase-locking in an ocean–atmosphere coupled model FGCM-1.0. *Adv. Atmos. Sci.*, **24**, 833–844, https://doi.org/10.1007/s00376-007-0833-z.

Zheng, Y., W. Chen, and S. Chen, 2021: Intermodel spread in the impact of the springtime Pacific meridional mode on following-winter ENSO tied to simulation of the ITCZ in CMIP5/CMIP6. *Geophys. Res. Lett.*, **48**, e2021GL093945, https://doi.org/10.1029/2021GL093945.

Zhou, S., G. Huang, and P. Huang, 2020: Excessive ITCZ but negative SST biases in the tropical Pacific simulated by CMIP5/6 models: The role of the meridional pattern of SST bias. *J. Climate*, **33**, 5305–5316, https://doi.org/10.1175/JCLI-D-19-0922.1.

Zhu, J., A. Kumar, and B. Huang, 2015: The relationship between thermocline depth and SST anomalies in the eastern equatorial Pacific: Seasonality and decadal variations. *Geophys. Res. Lett.*, **42**, 4507–4515, https://doi.org/10.1002/2015GL064220.